

---

Article

# Room Temperature syntheses of ZnO and its structure

Domenica Tommasa Donia <sup>1</sup>, Elvira Maria Bauer <sup>2</sup>, Mauro Missori <sup>3</sup>, Ludovica Roselli <sup>4</sup>, Daniele Cecchetti <sup>4</sup>, Pietro Tagliatesta <sup>4</sup>, Lorenzo Gontrani <sup>5,\*</sup>, Marilena Carbone <sup>2,4,\*</sup>

<sup>1</sup> Department of Surgical Science, University of Rome Tor Vergata, Via Montpellier 1, 00133, Rome, Italy

<sup>2</sup> Italian National Research Council – Institute of Structure of Matter (CNR-ISM), Via Salaria km 29.3, 00015 Monterotondo, RM, Italy

<sup>3</sup> Institute of Complex Systems, National Research Council (CNR-ISC) and Department of Physics, Sapienza University of Rome, Rome, Italy

<sup>4</sup> Department of Chemical Science and Technologies, University of Rome Tor Vergata, Via della Ricerca Scientifica 1 – 00133 Rome, Italy

<sup>5</sup> Department of Chemistry, Sapienza University of Rome, P.le A. Moro 2, Rome, 00185, Italy

\* Correspondence MC: Carbone@uniroma2.it

and

\* Correspondence LG: Lorenzo.Gontrani@uniroma1.it

**Abstract:** ZnO has many technological applications which largely depend on its properties that can be tuned by controlled synthesis. Ideally, the most convenient ZnO synthesis is carried out at room temperature in aqueous solvent. However, the correct temperature values are often loosely defined. In the current paper we performed synthesis of ZnO in aqueous solvent, by varying reaction and drying temperature by 10°C steps and monitored the synthesis products primarily by XRD. We found out that a simple direct synthesis of ZnO, without additional surfactant, pumping of freezing, required both a reaction ( $T_P$ ) and a drying ( $T_D$ ) temperature of 40°C. Higher temperatures also afford ZnO, but lowering any of the  $T_P$  or  $T_D$  below the threshold value results either in the achievement of Zn(OH)<sub>2</sub> or in a mixture of Zn(OH)<sub>2</sub>/ZnO. A more detailed Rietveld analysis of the ZnO samples reveals a density variation with the synthesis temperature and an increase of the nanoparticles average size also verified by SEM images. The optical properties of ZnO obtained by UV-Vis reflectance spectroscopy indicate a red shift of the band gap by ~0.1 eV.

**Keywords:** ZnO; Room Temperature Synthesis; XRD Characterization UV-Vis reflectance spectroscopy

---

## 1. Introduction

Metal and mixed metal and semiconductor oxides are widely applied in several fields, as supercapacitors [1,2,3], gas sensors based on chemoresistivity [4,5,6,7,8], or by using dielectric excitation [9,10], heterojunctions [11,12], energy storage as in batteries [13-15], and electrochemistry [16-18]. Their properties can be varied in different ways, by doping [19], capping, and controlling structure, shape and size, with bottom-up and top-down approaches [20-27]. Types of synthesis include sol-gel methods, hydrothermal synthesis, solvothermal synthesis, electrospinning [28-34]. Among the oxides, ZnO has been thoroughly investigated because of its properties, such as a wide band gap (~3.35 eV) with a high exciton binding energy of (~60 meV), wurtzite crystal structure, piezoelectric properties, and relatively low cost [35,36], which make it a suitable candidate for energy conversion/storage, high-performance electronics, photocatalysis, sensors, solar cells and supercapacitors [37-41]. In addition, it is applied in environmental remediation [42,43], as biocide and as nanofertilizer in agriculture [44,45].

The synthetic strategy and the careful control of synthesis parameters play a key role in determining the ZnO properties. In addition, environmentally friendly syntheses must be privileged, also on account of the extent of ZnO applications and consequent sizeability

of the production. Ideally, a green synthesis is performed at room temperature with water solvent and possibly a high yield. In this framework we reviewed the literature, in search of the optimum synthesis conditions. However, when exploring RT syntheses, it appeared that a quite large variety of parameters are included under the RT label, or that additional operations besides RT synthesis are required to achieve pure ZnO.

A common feature to all syntheses is the use of a large excess of base, typically NaOH, with respect to the Zn salt ( $\text{Zn}(\text{NO}_3)_2$ ,  $\text{Zn}(\text{CH}_3\text{CO}_2)_2$ ), from a minimum of 5 up to 50 times larger. Room temperature synthesis was carried out at 25°C, double jet conditions, controlling the shape and size of ZnO by pH of the solution (pH 9.5 to 10.5). In addition, a surfactant (sodium dodecyl sulfate) was used. Following operations require the precipitate to be washed with distilled water, frozen, and subsequently vacuum dried [46].

A synthesis was carried out at RT (exact value non specified) [47], by keeping the solution sealed and in dark up to 60 days, centrifuged, washed with water and ethanol and then dried under vacuum. XRD indicated the formation of ZnO, though spectra were reported starting from  $2\theta > 20^\circ$ , whereas signature reflexes of  $\text{Zn}(\text{OH})_2$  appeared very near to that boundary ( $2\theta=20.16^\circ$  and  $2\theta=20.89^\circ$ ) [48]. A synthesis of ZnO nanoparticles as well as micrometric agglomerates was performed at RT by using  $\text{Zn}(\text{CH}_3\text{CO}_2)_2$  and a mixture of NaOH and  $\text{NH}_4\text{F}$  in water solution in variable proportions. The reaction was carried out for 10 min, followed by centrifugation, washing with water and ethanol and drying at temperatures between 60°C and 75°C [49]. Sonochemistry was used for 10 min RT synthesis, followed by 2-4h sonication at 40 KHz, filtration, washing with methanol and drying also at RT [50]. In this case, the sonication procedure could be crucial, not only because of the ultrasound waves sent to the sample, but also for the temperature of the bath which tends to increase during the sonication, if not externally controlled. Syntheses at different temperatures by 10°C stepwise increase between 0°C and 80°C were carried out from  $\text{Zn}(\text{CH}_3\text{CO}_2)_2$  and NaOH water solutions, followed by centrifugation and washing with water. In this case the drying was achieved by lyophilization [51]. In all cases ZnO is reported as sole product, though XRD patterns start off at  $2\theta=0^\circ$ , and significant  $\text{Zn}(\text{OH})_2$  contributions are excluded. In a relatively quick synthetic procedure, ZnO was achieved at RT by precipitation, 30min stirring and 1h ageing. However, drying followed at 60°C, though the length of the latter is not mentioned [52].

A synthesis at RT is reported by Kumar et al. [53] where  $\text{NH}_4\text{OH}$  is added dropwise to a water solution of  $\text{Zn}(\text{NO}_3)_2$  of unspecified concentration under controlled, though not disclosed, pH and ensuing 48h RT drying.

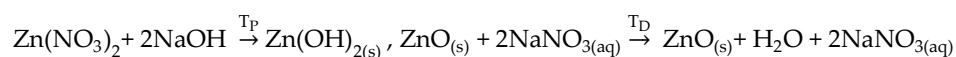
All-in-all, ZnO is either not fully achieved by carrying out operations solely at room temperature, or insufficient details are reported, or, simply, it is not always clear which the room temperature was during the synthetic procedure.

In the current paper, we explore the effects of “room temperature” on the achievement of ZnO and on its structure by carrying out syntheses in aqueous and controlling reaction and drying temperatures in steps of 10°C. The minimum temperature for synthesizing pure ZnO nanoparticles is 40°C, for both phases (reaction and drying), whereas at 30°C, only  $\text{Zn}(\text{OH})_2$  is achieved. At higher synthesis temperatures ZnO is also obtained, though of larger average size and slightly different volume density and cell parameters. The band gap of ZnO is consistent with the nanoparticle nature of the synthesized samples.

## 2. Materials and Methods

All chemicals were of reagent grade and used without any further purification.  $\text{Zn}(\text{NO}_3)_2$ , and NaOH were purchased from Sigma-Aldrich. All solutions were prepared with deionized water.

The syntheses were carried out according to the following reaction:



where  $T_P$  is the temperature of the precipitation reaction and  $T_D$  is the drying temperature. More in detail, a 0.1 M  $Zn(NO_3)_2$  solution was first prepared in deionized water and stirred for a few minutes until completely dissolved. Then, an equal volume of a 0.1 M NaOH solution was added dropwise to the solution normalized in oil bath at the selected temperature and stirred 24h.

In first instance, in the selection of the synthesis parameters, the ratio between  $Zn(NO_3)_2$  and NaOH was kept at 1:1, i.e. in excess of  $Zn^{2+}$ . This implies an initial pH of 6, that corresponds to a minimum of ZnO solubility in water (at 25°C) [54], to ensure that formed ZnO does not redissolve. In a typical synthesis, the reaction is carried out at a given temperature ( $T_P$ ), the slurry digested for two hours, centrifuged (3500 rpm for 10 min), washed with distilled water multiple times and then dried at the chosen temperature ( $T_D$ ) in an oven for 72 h. A white powder was, then, achieved, which was further characterized. The summary of the syntheses conditions is reported in Table 1.

**Table 1.** Samples Preparation Conditions.

Sample	Reaction Temperature	Drying Temperature
P30D30	30°C	30°C
P30D40	30°C	40°C
P40D40	40°C	40°C
P50D30	50°C	30°C
P50D50	50°C	50°C
P60D60	60°C	60°C

X-ray diffraction (XRD) patterns of the synthesized samples were collected with an X'pert pro X-ray diffractometer by Philips, using CuK-Alpha radiation. They were, then, analyzed by a Rietveld procedure with the GSAS-II suite of programs [55]. Scanning Electron micrographs (SEMs) were collected with a Zeiss Auriga 405, Field Emission-Scanning Electron Microscope instrument, mounting a Gemini column and operating at 7 kV.

Optical measurements in the ultraviolet (UV), visible (Vis), and near infrared (NIR) spectral regions were obtained by a diffuse reflectance setup from Avantes BV (The Netherlands). The latter comprises a combined deuterium-halogen radiation source (AvaLight-DH-S-BAL) connected via an optical fiber to a 30 mm-diameter Spectralon® coated integrating sphere (AvaSphere-30-REFL used to illuminate the samples (sampling port diameter 6 mm) and collect the radiation diffusely reflected from all angles. The ZnO powders were placed in the well of a sample holder with a depth such as to be able to consider the reflectance spectra as those of an infinitely thick sample ( $R_\infty$ ). The integrating sphere was connected through another optical fiber to a spectrometer (AvaSpec-2048x14-USB2). This configuration allows applications in the 248–1050 nm range with a 2.4 nm spectral resolution. A laptop is used for spectrometer control and data recording, whereas factory calibrated Spectralon® (Labsphere, USA), is used as reflectance reference. Each reflectance spectrum was obtained by averaging 5 acquisitions lasting 5 seconds each.

### 3. Results and Discussion

The solvo-synthesis of ZnO can be depicted as a two-stages process, i.e. precipitation and drying. The achievement of the ZnO, rather than  $Zn(OH)_2$  or a combination of the two moieties, strictly depends on the operational modalities of two stages.

In the present paper we opted for determining the best match in terms of temperature of each of the two steps, aiming at finding the lowest possible ones, which would

guarantee no detectable presence of  $\text{Zn}(\text{OH})_2$ . The verification of the composition was primarily carried out by XRD. Additional information on the fine structure of ZnO were determined by Rietveld refinement. A first synthesis was carried at  $T_{\text{r}}=T_{\text{d}}=30^\circ\text{C}$ , hence the closest, in our experimental setup, to the classical definition of  $\text{RT}=25^\circ\text{C}$ . In this setup we obtained nearly 100%  $\text{Zn}(\text{OH})_2$  samples (Figure 1). We, then, increased the drying temperature by  $10^\circ\text{C}$  to achieve the sample P30D40 and, subsequently, also the reaction temperature by  $10^\circ\text{C}$  (sample P40D40). The former setup still affords a mixture of ZnO and  $\text{Zn}(\text{OH})_2$ , whereas the XRD of the latter indicates the solely presence of ZnO. We also verified that a temperature of  $40^\circ\text{C}$  was strictly necessary to achieve ZnO, by varying the reaction temperature to  $50^\circ\text{C}$  and using either  $30^\circ\text{C}$  or  $40^\circ\text{C}$  for the drying procedure. Once more, the former yields a mixture of ZnO and  $\text{Zn}(\text{OH})_2$  whereas the latter is pure ZnO. Finally, we performed a synthesis at  $T_{\text{r}}=T_{\text{d}}=60^\circ\text{C}$  obtaining pure ZnO. Therefore, in general,  $40^\circ\text{C}$  is the threshold temperature necessary both for the reaction and for drying in order to achieve ZnO.

Since RT ZnO syntheses reported in literature are typically carried out in basic conditions, with  $\text{Zn}(\text{NO}_3)_2$  and NaOH ratio 1:5 to 1:50 [51-58] and  $\text{pH} \geq 12$ , we verified whether basic conditions would allow lower temperature conditions and carried out a synthesis using a  $\text{Zn}(\text{NO}_3)_2$ :NaOH ratio of 1:10, at  $T_{\text{p}}=T_{\text{d}}=30^\circ\text{C}$ . Also in this case we achieved  $\text{Zn}(\text{OH})_2$  (XRD not shown).

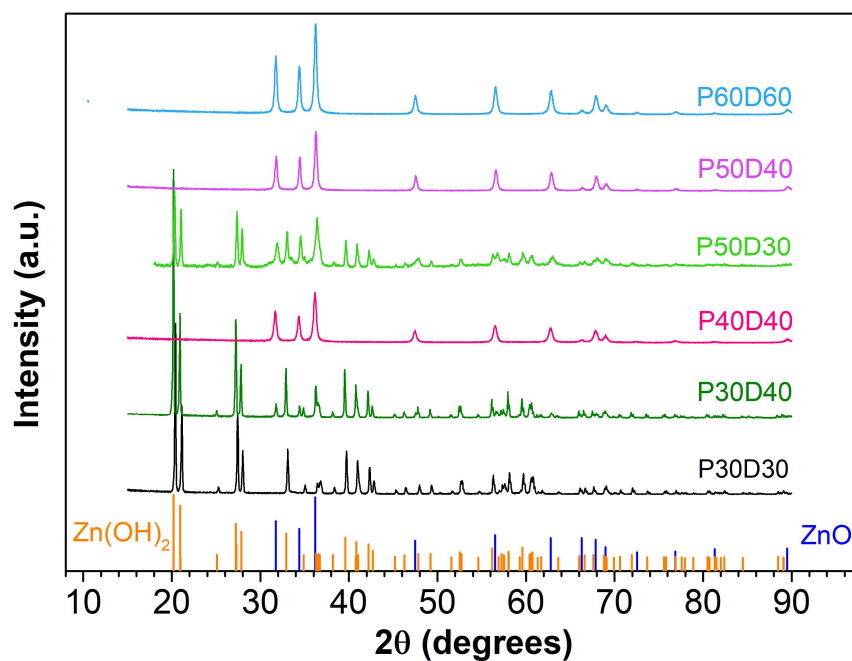


**Figure 1.** XRD patterns of the synthesized samples.

The powder X-Ray diffraction spectra of all the samples P30D30, P30D40, P40D40, P50D30, P50D40 and P60D60, were first visually compared (Figure 1) and then analyzed with Rietveld refinement using the GSAS-II software [55]. P40D40, P50D40 and P60D60 proved to be composed of pure ZnO, and the difference of the structural parameters was investigated, whereas P30D30, P30D40, and P50D30, on the contrary, turned out to contain both the target product (ZnO) and the precursor  $\text{Zn}(\text{OH})_2$ . For this reason, the relative composition of the two solid phases in the mixture was assessed besides the structural parameters. The preliminary qualitative comparison of the spectra pointed out that in P60D60, P50D40, P40D40- the first three patterns reported in Figure 1 - the peak positions are similar, the only notable difference being their intensity that is highest for P60D60 and comparable in the other two systems. A common crystal structure can

therefore be envisaged for them. A more accurate analysis, though, (see Figure 2), shows that the most intense peaks from P60D60 fall almost in the middle between P40D40 peaks (lower angle) and P50D50 ones (higher angle); the latter two sets of peaks are shifted by 0.1 degrees, on average.

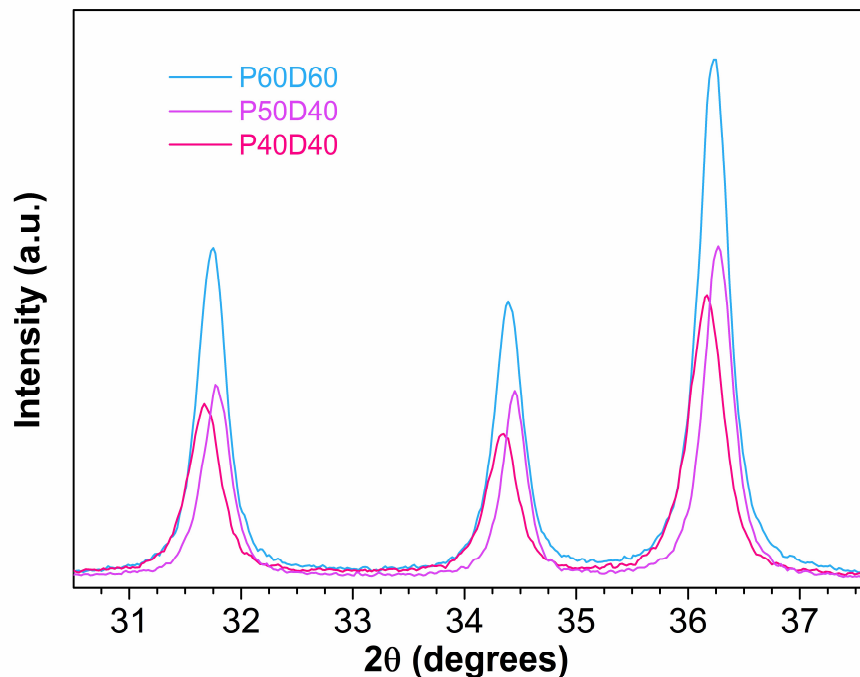


Figure 2. Details of pure zinc oxide samples XRD patterns

This issue suggests that a slight change of some crystal parameter(s) occurs among the three structures. Regarding P30D40, P30D30, and P50D30, the patterns are characterized by a large number of new peaks that show up in all angle ranges, especially the very intense ones before 30 degrees, a portion of the spectrum where no peaks are found in P60D60, P50D40 and P40D40. The crystal structures of the mineral zincite (100% ZnO, space group P63mc) [56] and of Wulffingite (pure zinc hydroxide, P212121) [48] were then employed in the fitting procedure. Both single-crystal phase data were downloaded from the American Mineralogist Crystal Structure Database [57] as Crystallographic Information Files (CIF). The simulated powder pattern for each sample was obtained, for CuK $\alpha$  wavelength (1.54 Å), modelling the peak shapes with a convolution of modified asymmetric pseudo-Voigt functions [58]. The background was modelled with a 3-term Chebyshev polynomial of the first kind. P60D60 profile was successfully fitted on 3100 observations, reaching the weighted-profile R factor wR = 11.76%, R=8.20%,  $\chi^2 = 5420.14$  at convergence. The same approach was adopted for the other systems, obtaining wR = 14.96%, R=10.83%,  $\chi^2 = 6382.69$  for P50D40; wR= 14.16%, R= 9.79%,  $\chi^2 = 5254.82$  for P40D40; wR= 24.82%, R= 17.94%,  $\chi^2 = 3188.23$  for P30D40, wR= 17.36 %, R= 13.09 %,  $\chi^2 = 15145.9$  for P30D30; wR= %, R= 17.36%,  $\chi^2 = 15153.9$  for CM9 and wR= 24.82%, R= 17.94% and  $\chi^2 = 3188.23$  for P50D30. The ratio between oxide and hydroxide phase fractions in the mixtures was fitted as well, obtaining the following ZnO:Zn(OH)<sub>2</sub> ratios: 22:78, 0.05:99.5, 85:15 and 69:31 for P30D40, P30D30 and P50D30 respectively. The fitting plots are reported in the Supplementary Information figures SI1 through SI6. The sample P30D30 will be from now on considered as pure hydroxide for simplicity. The fitting procedure also returns the optimized structural parameters for the cell(s) and the atom positions; additional fitted parameters were the domain size and microstrain of the crystallites, as well as the sample position and the instrumental broadening parameters U, V, W. The

most important parameters are reported in the tables below (Table 2 for pure ZnO, Table 3 for the mixtures).

**Table 2.** Pure ZnO systems. Fitted cell parameters, domain sizes and fractional coordinates

Sample	a (Å)	b (Å)	c (Å)	Volume (Å <sup>3</sup> )	Density (gcm <sup>-3</sup> )	Dom. Size (µm)
P40D40	3.24009	3.24009	5.20890	47.358	5.707	0.0469
P50D40	3.31864	3.31864	5.14557	49.078	5.507	0.0848
P60D60	3.27670	3.27670	5.20890	48.434	5.580	0.0791
Fractional coordinates	X (Zn)	Y (Zn)	Z (Zn)	X (O)	Y (O)	Z (O)
P40D40	0.33333	0.66667	-0.04651	0.33333	0.66667	0.34516
P50D40	0.33333	0.66667	-0.02259	0.33333	0.66667	0.36759
P60D60	0.33333	0.66667	-0.02279	0.33333	0.66667	0.36779

**Table 3.** Mixed ZnO/Zn(OH)<sub>2</sub> systems. Fitted cell parameters, domain sizes and fractional coordinates

Sample/Phase	a (Å)	b (Å)	c (Å)	Volume (Å <sup>3</sup> )	Density (gcm <sup>-3</sup> )	Dom. Size (µm)	Fraction		
P30D40									
ZnO	3.25866	3.25866	5.20629	47.878	5.645	0.0961	22.46%		
Zn(OH) <sub>2</sub>	4.90609	5.14418	8.47285	213.836	3.087	0.2682	77.54%		
Fractional coordinates	X(Zn)	Y (Zn)	Z (Zn)	X(O1)	Y (O1)	Z (O1)	X(O2)	Y (O2)	Z (O2)
ZnO	0.33333	0.66667	-0.01969	0.33333	0.66667	0.36469			
Zn(OH) <sub>2</sub>	0.07118	0.65017	0.62232	0.12575	0.12791	0.07742	0.18748	0.31445	0.72972
Sample/Phase	a (Å)	b (Å)	c (Å)	Volume (Å <sup>3</sup> )	Density (gcm <sup>-3</sup> )	Dom. Size (µm)	Fraction		
P30D30									
Zn(OH) <sub>2</sub>	4.66647	5.45967	8.36003	212.992	3.100	0.2865	≈100%		
Fractional coordinates	X(Zn)	Y (Zn)	Z (Zn)	X(O1)	Y (O1)	Z (O1)	X(O2)	Y (O2)	Z (O2)
Zn(OH) <sub>2</sub>	0.06814	0.65039	0.62453	0.11409	0.13244	0.08367	0.19477	0.31458	0.73196
Sample/Phase	a (Å)	b (Å)	c (Å)	Volume (Å <sup>3</sup> )	Density (gcm <sup>-3</sup> )	Dom. Size (µm)	Fraction		
P50D30									
ZnO	3.24544	3.24544	5.20182	47.450	5.696	0.0392	68.98%		
Zn(OH) <sub>2</sub>	4.89683	5.13368	8.45536	212.557	3.106	10.0	31.02%		
Fractional coordinates	X(Zn)	Y (Zn)	Z (Zn)	X(O1)	Y (O1)	Z (O1)	X(O2)	Y (O2)	Z (O2)
ZnO	0.33333	0.66667	-0.02452	0.33333	0.66667	0.36952			
Zn(OH) <sub>2</sub>	0.06752	0.64093	0.62973	0.13339	0.11871	0.09189	0.15829	0.35522	0.71823

An interesting feature pointed out during the refinement was the difference in the cell parameters of the three pure zinc oxide samples. The cell parameters refinement confirms that P60D60 has an intermediate behavior with respect to P50D40 and P40D40. The cell dimensions and the resulting volume (and density) fall in the middle of the range, in compliance with the peak positions already discussed above. The density order P40D40 > P60D60 > P50D40 is nicely anticorrelated with the position of the peaks, i. e.

P40D40, the densest structure, having structural correlations that occur at smaller distance on average, gives origin to diffraction peaks that fall at larger angles (according to the scattering vector and Bragg's law definitions  $Q=4\pi\sin\theta/\lambda$  and  $d=2\pi/Q$  [59,60]) while the distances between the atoms contained in the least dense sample (P50D40) are typically larger and the resulting peaks fall at smaller angle. Interestingly, the cell dimensions are proportional to the average (fitted) dimension of the crystallites, signaling that smaller nanoparticles (P40D40) occupy the smallest volume, i.e. they are more efficiently packed. When compared with the single-crystal cell dimensions ( $a=3.24950$   $c=5.2069$ ), or with some recently reported ZnO nanosheets ( $a= 3.245$   $c=5.198$ , [61]), the first two nanoparticle samples appear to be significantly less dense, while P40D40 values are much closer. The calculated density values confirm this trend and satisfactorily comply with the experimental density value of  $5.61 \text{ g cm}^{-3}$  [62]. The modulation of the structural features observed demonstrates that our synthesis protocol, by a simple tuning of the temperature, is capable of leading, easily and successfully, to final products with different properties.

The synthesized samples display different types of morphology, depending on the temperature adopted in the different phases of the synthesis. Examples of the morphology of the samples are reported in Figure 3. The P30D30 sample, mostly composed of  $\text{Zn}(\text{OH})_2$ , has micrometric structure of aggregated foils. In the P30D40 sample the micrometric arrangements become more compact to form blocks and some nanoparticles appear on their surface highlighted in Figure 3b with light orange circles. Once pure ZnO is formed, i.e. when both reaction and drying temperatures are, at least,  $40^\circ\text{C}$ , the samples are characterized by the shear presence of nanoparticles. The nanoparticle morphology of ZnO is kept also for higher synthesis temperature, though the average size is slightly larger. In particular, the average size of the P40D40, P50D40 and P60D60 are  $53\pm 10$  nm,  $65\pm 12$  nm and  $69\pm 11$  nm, respectively, thus in agreement with the crystallite size detected by XRD, within the experimental error. In addition, there is a good agreement between estimated crystallite size and the samples morphology, for mixed  $\text{Zn}(\text{OH})_2/\text{ZnO}$  samples with larger average size associated to  $\text{Zn}(\text{OH})_2$  as compared to ZnO. XRD allows a separate assessment of the average size of each phase. Though this is not possible by SEM imagining, since the morphology cannot quite distinguish the crystallographic phase, it can be hypothesized that the small nanoparticles on the surface of the blocks in the P30D40 sample are actually ZnO deriving from the  $\text{Zn}(\text{OH})_2$  dehydration.

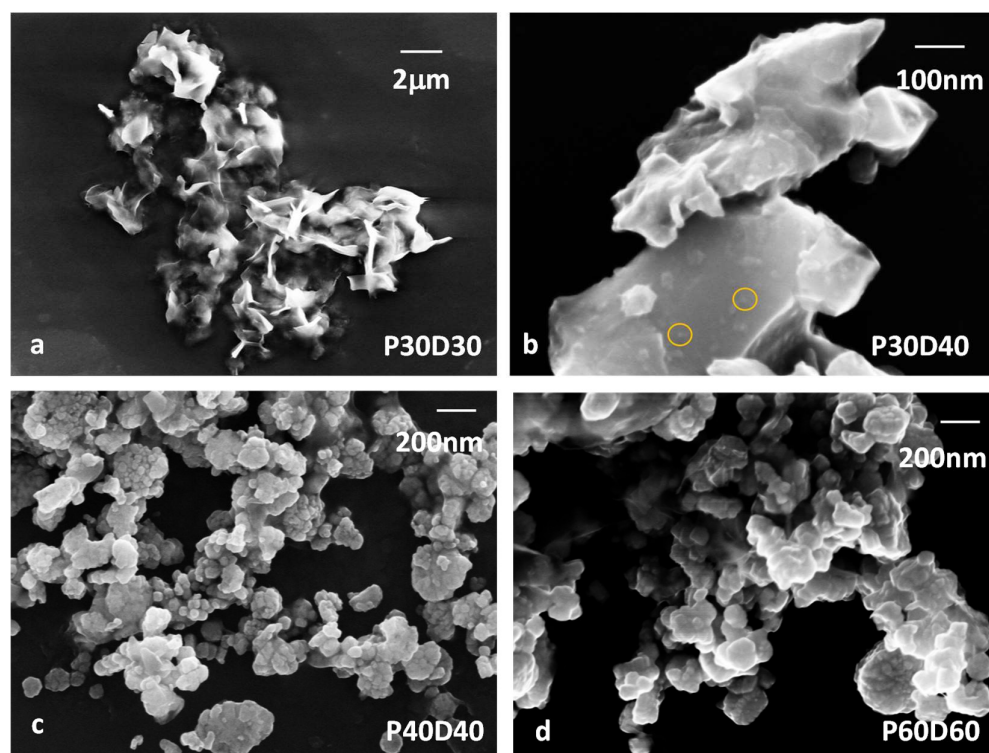


**Figure 3.** Selected SEM images of the synthesized samples: a) P30D30, b) P30D40, c) P40D40, d) P60D60.

The band gap of the ZnO nanoparticles samples was estimated by diffuse reflectance  $R_\infty$  spectra, where  $R_\infty$  is the reflectance of an infinitely thick layer of sample, converted into absorption spectra by using the Kubelka-Munk function [63,64]:

$$\frac{K}{S} \equiv \frac{(1 - R_\infty)^2}{2R_\infty}$$

where  $K$  and  $S$  are the Kubelka–Munk absorption and scattering coefficient, respectively... The  $K$  absorption coefficient is related to the intrinsic absorption coefficient of the particles  $\alpha$  by  $\alpha = K/2$ , in case of diffuse light distribution as in our case [65]. The steady preparation of ZnO powder sample for optical measurements also allowed us to consider  $S$  constant from sample to sample, then the ratio  $K/S \approx \alpha$ . In order to estimate the band gap from the absorption spectra we can, then, apply the Tauc relation [66]:

$$\alpha h\nu = C1(h\nu - E_g)^n$$

Where  $n=1/2$  for indirect gap and  $n=2$  for direct gaps, such as the case of ZnO, and  $C1$  is a constant.

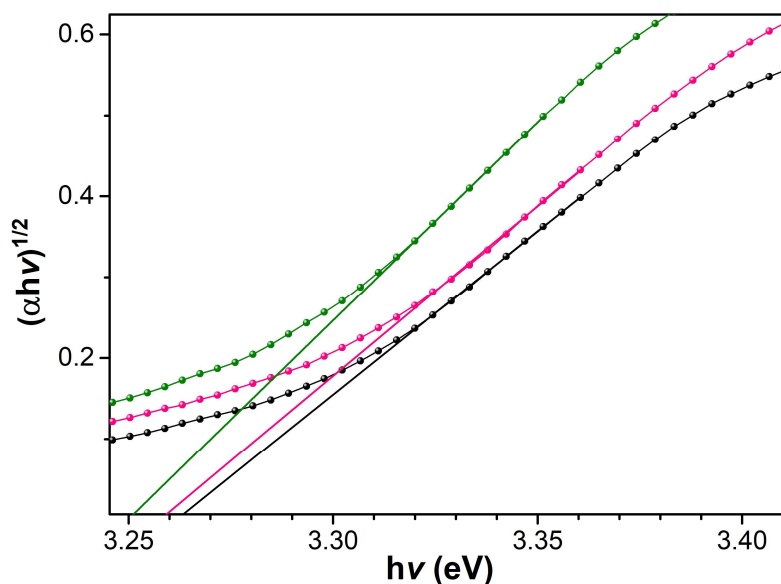


**Figure 4.** Tauc plots for the determination of optical band gap  $E_g$  (lines+dots) and associated extrapolations of the linear regions (solid lines). Green corresponds to the sample P40D40, red to P50D40 and black to P60D60.

The ZnO band gap  $E_g$  including the quantum confinement as a function of the average particle size is obtained from the effective mass model given by [67,68]:

$$E_g \cong E_g^{bulk} + \frac{h^2}{8e\mu r^2} - \frac{1.8e}{4\pi\epsilon_r\epsilon_0 r} - \frac{0.124e^3\mu}{(2h\epsilon_r\epsilon_0)^2}$$

In this equation all terms are in eV,  $E_g^{bulk}$  is the bulk ZnO band gap (3.35 eV),  $h$  is the Planck constant,  $r$  is the particle radius,  $e$  is the charge of the electron,  $\mu$  is the reduced mass of electron and holes  $\mu = \frac{m_e^*m_h^*}{m_e^*+m_h^*}$ , where  $m_e^*$  and  $m_h^*$  are the effective mass of the electrons and holes in ZnO, respectively,  $m_e^* = 0.19m_e$  and  $m_h^* = 0.8m_e$ , where  $m_e$  is the free electron mass [69];  $\epsilon_r$  (3.7) is the relative permittivity,  $\epsilon_0$  is the permittivity of free space.

The  $E_g$  values of 3.25(0), 3.25(8) and 3.26(2) eV (Table 4) injected in the previous equation all yields nanoparticles sizes ( $2r$ ) of about 15 nm, providing an estimation of the smaller size in the synthesized ZnO nanoparticles.

**Table 4.** Band gap of the ZnO samples.

Sample	Band Gap (eV)
P40D40	3.25(0)
P50D40	3.25(8)
P60D60	3.26(2)

Compared to a band gap of 3.35 eV in bulk ZnO [70], P40D40, P50D40, P60D60 exhibit a red shift by  $\sim 0.1$  eV. ZnO nanoparticles, in general, may undergo both a blue and a red shift, many factors concurring to the actual band gap value. As shown by Eq. 1, below 14 nm diameter threshold, the size effect is dominant and a blue shift is observed [71,72]. However, also the shape plays a role and both red and blue shift, depending on the particles morphology, as determined by the employment of different solvents during the synthesis [73]. In RT synthesis followed by lyophilization, a red shift by  $\sim 0.1$  eV has been

observed between synthesis at 20°C and at 50°C and it has been associated to a slight size increase of the nanoparticles [51]. However a simultaneous shape change was also observed from elliptical to conical which may also contribute to the red shift. P40D40, P50D40, P60D60 have similar morphologies and the comparable band gap values would indicate similar average sizes. Comparison with XRD results, which give domain sizes ranging from 46.9 to 84.8 nm, suggests a shape anisotropy for the P40D40, P50D40 and P60D60 nanoparticles, which can be also observed from SEM images (Figure 3 c and d). It must be added that the average particles size in band gap corresponds to the pathway for an electronic transition through a gap, which can be equivalent for anisotropic samples, with similar minimum size pathway.

#### 4. Conclusions

Room temperature synthesis of ZnO nanoparticles in aqueous solution has been achieved. The synthesis has been carried out by controlling reaction and drying temperature, without the aid of any surfactant, pumping or freezing. We found out that the minimum temperature for achieving ZnO is 40°C for both synthetic phases. Lowering any of the two temperatures results in the achievement of Zn(OH)<sub>2</sub> or a mixture Zn(OH)<sub>2</sub>/ZnO. Beyond the threshold value of 40°C, ZnO nanoparticles are still obtained, though with larger average size and different density. The morphology is similar for all ZnO nanoparticles as well as the optical band gap. The morphology of lower temperature samples indicates the presence of aggregated foils, which merge to form blocks, from which ZnO nanoparticles eventually detach. The results obtained from SEM experiments comply quite well with X-Ray diffraction experiments and optical analysis of the band gap, where it was found that the scattering patterns observed for the samples synthesized at temperatures larger than 40°C show a shape anisotropy and an evident shift towards smaller angles, thus indicating systems of larger average dimensions and crystallites size.

**Supplementary Materials:** Figures S1 through SI6: XRD patterns of the samples P30D30, P30D40, P40D40, P50D30, P50D40, P60D60 and associated Rietveld fits.

**Author Contributions:** M.C. and D.D.; methodology, D.D., M.M.; software, M.M., L.R.; validation, L.R., D.D., M.M.; formal analysis, E.B.; investigation, D.D., L.R., M.M., E.B.; resources, M.C.; data curation, D.C., P.T.; writing—original draft preparation, M.C., L.G.; writing—review and editing, M.C., L.G.; supervision, M.C.; project administration, M.C. All authors have read and agreed to the published version of the manuscript.

**Acknowledgments:** The authors thank F. Mura from CNIS (Sapienza University of Rome) for his contribution to SEM characterization of the images.

**Conflicts of Interest:** The authors declare no conflict of interest.

#### References

1. Keimer, B.; Kivelson, S.A.; Norman, M.R.; Uchida, S.; Zaanen J. From quantum matter to high-temperature superconductivity in copper oxides. *Nature* **518**, **2015**, 179–186.
2. Rijckaert, H.; Pollefeyt, G.; Sieger, M.; Hänisch, J.; Bennowitz, J.; De Keukeleere, K.; De Roo, J.; Hühne, R.; Bäcker, M.; Paturi, P.; Huhtinen, H.; Hemgesberg, M.; Van Driessche, I. Optimizing Nanocomposites through Nanocrystal Surface Chemistry: Superconducting YBa<sub>2</sub>Cu<sub>3</sub>O<sub>7</sub> Thin Films via Low-Fluorine Metal Organic Deposition and Preformed Metal Oxide Nanocrystals. *Chem. Mater.* **2017**, *29*(14), 6104–6113.
3. Chakhalian, J.; Liu, X.; Fiete, G.A. Strongly correlated and topological states in [111] grown transition metal oxide thin films and heterostructures editors-pick. *APL Materials* **2020**, *8*, 050904.
4. Neri, G. First Fifty Years of Chemoresistive Gas Sensors. *Chemosensors* **2015**, *3*(1), 1–20;
5. Carbone, M. CQDs@NiO: An efficient tool for CH<sub>4</sub> sensing. *Appl. Sci.* **2020**, *10*(18), 6251.
6. Sturaro, M.; Della Gaspera, E.; Michieli, N.; Cantalini, C.; Emamjomeh, S.M.; Guglielmi, M.; Martucci, A. Degenerately Doped Metal Oxide Nanocrystals as Plasmonic and Chemoresistive Gas Sensors. *ACS Appl. Mater. Interfaces* **2016**, *8*(44), 30440–30448.

- 
7. Lin, T.; Lv, X.; Hu, Z.; Xu, A.; Feng, C. Semiconductor Metal Oxides as Chemoresistive Sensors for Detecting Volatile Organic Compounds *Sensors* **2019**, *19*(2), 233.
  8. Carbone, M.; Tagliatesta, P. NiO grained-flowers and nanoparticles for ethanol sensing. *Materials*, **2020**, *13*(8), 1880.
  9. Potyrailo, R.A.; Go, S.; Sexton, D.; Li, X.; Alkadi, N.; Kolmakov, A.; Amm, B.; St-Pierre, R.; Scherer, B.; Nayeri, M.; Wu, G.; Collazo-Davila, C.; Forman, D.; Calvert, C.; Mack, C.; McConnell, P. Extraordinary performance of semiconducting metal oxide gas sensors using dielectric excitation. *Nat. Electron.* **2020**, *3*, 80-289.
  10. Lee H.J. Linear gas sensing with dielectric excitation. *Nat. Electron.* **2020**, *3*, 239-240.
  11. Yao, Y.; Sang, D.; Duan, S.; Wang, Q.; Liu, C. Review on the Properties of Boron-Doped Diamond and One-Dimensional-Metal-Oxide Based P-N Heterojunction *Molecules* **2021**, *26*(1), 71.
  12. Staerz, A.; Gao, X.; Cetmi, F.; Ming, Z.; Weimar, U.; Zhang, T.; Barsan N. Dominant Role of Heterojunctions in Gas Sensing with Composite Materials, *ACS Appl. Mater. Interfaces* **2020**, *12*, 21127–21132.
  13. Carbone, M. Zn defective ZnCo<sub>2</sub>O<sub>4</sub> nanorods as high capacity anode for lithium ion batteries. *J. Electroanal. Chem.* **2018**, *815*, 151-157.
  14. Fang, S.; Bresser, D.; Passerini S. Transition Metal Oxide Anodes for Electrochemical Energy Storage in Lithium- and Sodium-Ion Batteries, *Adv. Energy Mater.* **2020**, *10*, 1902485.
  15. Li, Q.; Li, H.; Xia, Q.; Hu, Z.; Zhu, Y.; Yan, S.; Ge, C.; Zhang, Q.; Wang, X.; Shang, X.; Fan, S.; Long, Y.; Gu, L.; Miao, G.-X.; Yu, G.; Moodera, J.S. Extra storage capacity in transition metal oxide lithium-ion batteries revealed by in situ magnetometry. *Nat. Mater.* **2021**, *20*, 76-83.
  16. Carbone, M.; Nesticò, A.; Bellucci, N.; Micheli, L.; Palleschi, G. Enhanced performances of sensors based on screen printed electrodes modified with nanosized NiO particles. *Electrochim. Acta*, **2017**, *246*, 580-587.
  17. Agnihotri, A.S.; Varghese, A.; Nidhin, M. Transition metal oxides in electrochemical and bio sensing: A state-of-art review, *Appl. Surf. Sci. Adv.* **2021**, *4*, 100072.
  18. Valentini, F.; Roscioli, D.; Carbone, M.; Conte, V.; Floris, B.; Palleschi, G.; Flammini, R.; Bauer, E.M.; Nasillo, G.; Caponetti, E. Oxidized graphene in ionic liquids for assembling chemically modified electrodes: A structural and electrochemical characterization study. *Anal. Chem.* **2012**, *84*(13), 5823-5831.
  19. Stankic, S.; Suman, S.; Haque, F.; Vidic J. Pure and multi metal oxide nanoparticles: synthesis, antibacterial and cytotoxic properties *J. Nanobiotechnol.* **2016**, *14*, 73.
  20. Zhang, W.; Li, J.; Zhang, J.; Sheng, J.; He, T.; Tian, M.; Zhao, Y.; Xie, C.; Mai, L.; Mu S. Top-Down Strategy to Synthesize Mesoporous Dual Carbon Armored MnO Nanoparticles for Lithium-Ion Battery Anodes, *ACS Appl. Mater. Interfaces*, **2017**, *9*(14), 12680–12686.
  21. Casaletto, M.P.; Zanoni, R.; Carbone, M.; Piancastelli, M.N.; Aballe, L.; Weiss, K.; Horn, K. Ethylene adsorption on Si(100)2×1: A high-resolution photoemission study. *Phys. Rev. B*, **2000**, *62*, 17128-17133.
  22. Li, F.; Ran, J.; Jaroniec, M.; Qiao S. Z. Solution combustion synthesis of metal oxide nanomaterials for energy storage and conversion, *Nanoscale*, **2015**, *7*, 17590-17610.
  23. Carbone, M.; Caminiti, R. Adsorption states and site conversions of phenylacetylene on Si(100)2 × 1 calculated by DFT. *J. Theor. Comput. Chem.* **2012**, *11*(5), 1089-1099.
  24. Ortega, S.; Ibáñez, M.; Liu, Y.; Zhang, Y.; Kovalenko, M.V.; Cadavid, D.; Cabot, A. Bottom-up engineering of thermoelectric nanomaterials and devices from solution-processed nanoparticle building blocks. *Chem. Soc. Rev.* **2017**, *46*, 3510-3528.
  25. Carbone, M.; Piancastelli, M.N.; Casaletto, M.P.; Zanoni, R.; Besnard-Ramage, M.J.; Comtet, G.; Dujardin, G.; Hellner, L. Phenol adsorption on Si (111)7 × 7 studied by synchrotron radiation photoemission and photodesorption. *Surf. Sci.* **1999**, *419*, 114-119.
  26. de Oliveira, P.F.M.; Torresi, R.M. Emmerling, F.; Camargo, P.H.C. Challenges and opportunities in the bottom-up mechanochemical synthesis of noble metal nanoparticles *J. Mater. Chem. A*, **2020**, *8*, 16114-16141.
  27. Gontrani, L., Tagliatesta, P., Agresti, A., Pescetelli, S., Carbone, M. New insights into the structure of glycols and derivatives: A comparative x-ray diffraction, raman and molecular dynamics study of ethane-1,2-diol, 2-methoxyethan-1-ol and 1,2-dimethoxy ethane. *Crystals* **2020**, *10*(11), 1011.
  28. Mondal, K. Recent Advances in the Synthesis of Metal Oxide Nanofibers and Their Environmental Remediation Applications, *Inventions* **2017**, *2*, 9.
  29. Carbone, M. Cu-Zn-Co nanosized mixed oxides prepared from hydroxycarbonate precursors. *J. Alloy. Compd.* **2016**, *688*, 202-209.
  30. Chen, Y.; Lu, W.; Guo, Y.; Zhu, Y.; Lu, H.; Song, Y. Synthesis, Characterization and Photocatalytic Activity of Nanocrystalline First Transition-Metal (Ti, Mn, Co, Ni and Zn) Oxide Nanofibers by Electrospinning. *Appl. Sci.* **2019**, *9*, 8.
  31. Carbone, M.; Bauer, E.M., Micheli, L.; Missori, M. NiO morphology dependent optical and electrochemical properties, *Colloid. Surface. A*, **2017**, *532*, 178-182.

- 
32. Atchison, J.S.; Zeiger, M.; Tolosa, A.; Funke, L.M.; Jackel, N.; Presser V. Electrospinning of ultrafine metal oxide/carbon and metal carbide/carbon nanocomposite fibers, *RSC Adv.* **2015**, *5*, 35683–35692.
33. Carbone, M.; Missori, M.; Micheli, L.; Tagliatesta, P.; Bauer, E.M. NiO pseudocapacitance and optical properties: Does the shape win? *Materials*, **2020**, *13*(6), 1417.
34. Xia, X.; Zhang, Y.; Chao, D.; Guan, C.; Zhang, Y.; Li, L.; Ge, X.; Mínguez Bacho, I.; Tu, J.; Fan, H.J. Solution synthesis of metal oxides for electrochemical energy storage applications. *Nanoscale*, **2014**, *6*, 5008-5048.
35. Djurišić, A.B.; Chen, X.; Leung, Y.H.; Ching Ng, A.M. ZnO nanostructures: growth, properties and applications. *J. Mater. Chem.* **2012**, *22*, 6526-6535.
36. Wang, J.; Chen, R.; Xiang, L.; Komarneni S. Synthesis, properties and applications of ZnO nanomaterials with oxygen vacancies: A review *Ceram. Int.*, **2018**, *44*, 7357-7377.
37. Son, D.-Y.; Im, J.-H.; Kim, H.-S.; Park N.-G. Efficient perovskite solar cell based on ZnO nanorods: an effective charge collection system. *J. Phys. Chem. C* **2014**, *118*, 16567-16573.
38. Wang, X.; Sun, F.; Duan, Y.; Yin, Z.; Luo, W.; Huang, Y.; Chen J. Highly sensitive, temperature-dependent gas sensor based on hierarchical ZnO nanorod arrays. *J. Mater. Chem. C* **2015**, *3*, 11397-11405.
39. Lee, K.M.; Lai, C.W.; Ngai, K.S.; Juan, J.C. Recent developments of zinc oxide based photocatalyst in water treatment technology: a review. *Water Res.* **2016**, *88*, 428-448.
40. He, Y.-B.; Li, G.-R.; Wang, Z.-L.; Su, C.-Y.; Tong Y.-X. Single-crystal ZnO nanorod/amorphous and nanoporous metal oxide shell composites: controllable electrochemical synthesis and enhanced supercapacitor performances. *Energy Environ. Sci.* **2011**, *4*, 1288-1292.
41. Ong, C.B.; Ng, L.Y.; Mohammad, A.W. A review of ZnO nanoparticles as solar photocatalysts: Synthesis, mechanisms and applications. *Renew. Sustain. Ener. Rev.* **2018**, *81*, 536–551.
42. Ammar, S.H.; Abdunabi, W.A.; Abdul kader H.D. Synthesis, characterization and environmental remediation applications of polyoxometalates-based magnetic zinc oxide nanocomposites (Fe<sub>3</sub>O<sub>4</sub>@ZnO/PMOs) *Environ. Nanotech. Monitor. Manag.* **2020**, *13*, 100289.
43. Donia, D.T.; Carbone M. Fate of the nanoparticles in environmental cycles, *Int. J. Environ. Sci. Technol.* **2019**, *16*(1), 583-600.
44. Carbone, M.; Briancesco, R.; Bonadonna, L. Antimicrobial power of Cu/Zn mixed oxide nanoparticles to *Escherichia coli*. *Environ. Nanotech. Monitor. Manag.* **2017**, *7*, 97-102.
45. Sheoran, P.; Grewal, S.; Kumari, S.; Goel, S. Enhancement of growth and yield, leaching reduction in *Triticum aestivum* using biogenic synthesized zinc oxide fertilizer, *Biocatal. Agricult. Biotechnol.* **2021**, *32*, 101938.
46. Oliveira, A.P.A.; Hochepeid, J.-F.; Grillon, F.; Berger, M.-H. Controlled Precipitation of Zinc Oxide Particles at Room Temperature. *Chem. Mater.* **2003**, *15*, 3202-3207.
47. Cao, H.L.; Qian, X.F.; Gong, Q.; Du, W.M. Ma, X.D.; Zhu, Z.K. Shape- and size-controlled synthesis of nanometre ZnO from a simple solution route at room temperature *Nanotechnology* **2006**, *17*, 3632–3636.
48. Stahl, R.; Jung, C.; Lutz, H. D.; Kockelmann, W, Jacobs, H. Kristallstrukturen und Wasserstoffbrückenbindungen bei  $\beta$ -Be(OH)<sub>2</sub> und  $\epsilon$ -Zn(OH)<sub>2</sub>. *Z. anorg. allg. Chem.* **1998**, *624*, 1130-1136
49. Wang, M.; Zhang, Y.; Zhou, Y.; Yang, F.; Kim, E.J.; Hahn, S.H.; Seong, S.G. Rapid room-temperature synthesis of nanosheet assembled ZnO mesocrystals with excellent photocatalytic activity. *Cryst. Eng. Comm.* **2013**, *15*, 754-763.
50. Wahab, R.; Ansari, S.G.; Kim, Y.-S.; Seo, H.-K.; Shin, H.-S. Room temperature synthesis of needle-shaped ZnO nanorods via sonochemical method. *App. Surf. Sci.* **2007**, *253*, 7622–7626.
51. Jaber, B.; Laânab, L. One step synthesis of ZnO nanoparticles in free organic medium: Structural and optical characterizations. *Mat. Sci. Semicon. Proc.* **2014**, *27*, 446–451.
52. Li, S.-M.; Zhang, L.-X.; Zhu, M.-Y.; Ji, G.-J.; Zhao, L.-X.; Yin, J.; Bie, L.-J. Acetone sensing of ZnO nanosheets synthesized using room-temperature precipitation. *Sensor. Actuat. B-Chem.* **2017**, *249*, 611–623.
53. Kumar, V.R.; Wariar, P.R.S.; Prasad, V.S.; Koshy, J. A novel approach for the synthesis of nanocrystalline zinc oxide powders by room temperature co-precipitation method. *Mater. Lett.* **2011**, *65*, 2059–2061.
54. Liu, Y.; Gao W. Growth process, crystal size and alignment of ZnO nanorods synthesized under neutral and acid conditions, *J. Alloys Compd.* **2015**, *629*, 84-91.
55. Toby BH, Von Dreele RB, GSAS-II: the genesis of a modern open-source all purpose crystallography software package, *J Appl Cryst* **2013**, *46*, 544-549
56. Xu, Y. N.; Ching, W. Y.; Electronic, optical, and structural properties of some wurtzite crystals. *Phys. Rev. B* **1993**, *48*, 4335-4351
57. Downs, R.T. Hall-Wallace, M. The American Mineralogist Crystal Structure Database. *Am. Mineral.* **2003**, *88*, 247-250
58. Finger L. W., Cox D. E., Jephcoat A. P. A correction for powder diffraction peak asymmetry due to axial divergence, *J Appl Cryst* **1994**, *27*(6), 892-900.

- 
59. Warren, B. E. X-Ray Diffraction (Dover, United Kingdom, 1990).
60. Campetella, M.; Mariani, A.; Sadun, C.; Wu, B.; Castner, E. W. Jr.; Gontrani, L. Structure and dynamics of propylammonium nitrate-acetonitrile mixtures: An intricate multi-scale system probed with experimental and theoretical techniques, *J. Chem. Phys.* **2018**, *148*, 134507 (2018)
61. Si-Meng, L.; Zhang, L-X; Meng-Ya, Zhu, M. Y.; Ji, G. J.; Zhao, L. X.; Yin J.; Bie, L- J, Acetone sensing of ZnO nanosheets synthesized using room-temperature precipitation, *Sens. Act. B* **2017**, *249*, 611–623
62. Haynes, W.M. (ed.). *CRC Handbook of Chemistry and Physics. 94th Edition*. CRC Press LLC, Boca Raton: Florida, United States), **2013-2014**, pp. 4-100.
63. Kubelka, P.; Munk, F.; Ein Beitrag Zur Optik Der Farbanstriche, *Z. Tech. Phys.* **1931**, *12*, 593-601.
64. Missori, M.; Pulci, O.; Teodonio, L.; Violante, C.; Kupchak, I.; Bagniuk, J.; Łojewska, J.; Mosca Conte, A.; Optical response of strongly absorbing inhomogeneous materials: Application to paper degradation, *Phys. Rev. B* **2014**, *89*, 054201.
65. Missori, M.; Optical spectroscopy of ancient paper and textiles, *Il nuovo Cimento C*, **2016**, *39*, 293.
66. Smith, R.A.; Semiconductors, 2<sup>nd</sup> ed., Cambridge University Press, Cambridge, **1978**.
67. Brus, L.E. Electron–electron and electron-hole interactions in small semiconductor crystallites: The size dependence of the lowest excited electronic state. *J. Chem. Phys.* **1984**, *80*:9, 4403-4409.
68. Sayari, A. Characterization of nanocrystalline ZnO flakes synthesized by a simple reaction process, *KONA Powder Part. J.* **2013**, *30*, 119-124.
69. Repp, S.; Erdem, E. Controlling the exciton energy of zinc oxide (ZnO) quantum dots by changing the confinement conditions, *Spectrochim. Acta A* **2016**, *152*, 637–644.
70. Studenikin, S.A.; Golego, N.; Cocivera, M. Fabrication of green and orange photoluminescent, undoped ZnO films using spray pyrolysis. *J. Appl. Phys.* **1998**, *84*, 2287.
71. Debanath, M.K.; Karmakar S. Study of blue shift of optical band gap in zinc oxide (ZnO) nanoparticles prepared by low-temperature wet chemical method. *Mater. Lett.* **2013**, *111*, 116–119.
72. Lin, K.-F.; Cheng, H.-M.; Hsu, H.-C.; Lin, L.-J.; Hsieh, W.-F. Band gap variation of size-controlled ZnO quantum dots synthesized by sol–gel method. *Chem. Phys. Lett.* **2005**, *409*, 208–211.
73. Davis, K.; Yarbrough, R.; Froeschle, M.; White, J.; Rathnayake, H.; Band gap engineered zinc oxide nanostructures via a sol–gel synthesis of solvent driven shapecontrolled crystal growth *RSC Adv.* **2019**, *9*, 14638-14648.